



Cite this: DOI: 10.1039/d5ta03354c

# Insights into the giant magnetocaloric effect in $\text{BiCu}_3\text{Cr}_4\text{O}_{12}$ with charge–spin–lattice coupling

Hung Ba Tran,<sup>id</sup>\*<sup>a</sup> Hao Li,<sup>id</sup>\*<sup>a</sup> Masato Goto,<sup>d</sup> Kazunori Sato<sup>bc</sup>  
and Yuichi Shimakawa<sup>id</sup><sup>d</sup>

The novel magnetocaloric effect of  $\text{BiCu}_3\text{Cr}_4\text{O}_{12}$  is comprehensively investigated, revealing the intricate interplay of charge–spin–lattice coupling. Using first-principles calculations, this study examines charge disproportionation and phonon properties, uncovering the fundamental mechanisms behind structural and electronic instability, as well as strong correlations in the electronic, lattice, and magnetic interactions of the material. Magnetic exchange coupling constants are systematically derived for two distinct crystallographic phases: the low-temperature  $C2/m$  phase and the high-temperature  $Im\bar{3}$  phase. By incorporating the classical Heisenberg model and a mixed-phase model, this work explores the mechanism of the first-order magnetic phase transition coupled with structural transformation. The giant isothermal magnetic entropy changes are successfully reproduced using Maxwell relations for the total magnetization of mixed phases, demonstrating the accuracy of our models and methods. Additionally, applying the Clausius–Clapeyron equation to the isothermal entropy change highlights the critical role of lattice, electronic, and magnetic contributions in the magnetocaloric effect. These findings illustrate how strong charge, spin, and lattice correlations in  $\text{BiCu}_3\text{Cr}_4\text{O}_{12}$  significantly enhance the isothermal entropy change compared to the isothermal magnetic entropy change with only the magnetic contribution. This study not only deepens the understanding of magnetocaloric materials but also offers valuable insights for developing energy-efficient refrigeration technologies.

Received 28th April 2025  
Accepted 29th July 2025

DOI: 10.1039/d5ta03354c

rsc.li/materials-a



Hung Ba Tran

*Hung Ba Tran is currently an Assistant Professor at the Advanced Institute for Materials Research (WPI-AIMR), Tohoku University, Japan (2024–now). He received his PhD degree in engineering from Osaka University, Japan (2018–2021), and his MEng degree in engineering from Osaka University, Japan (2017–2018). His doctoral thesis focused on applying computational materials science to study various types of magnetocaloric*

*effects, including conventional, giant, inverse, and anisotropic effects. His current research interests include magnetocaloric materials, permanent magnets, 2D materials, and transition-metal oxides, with an emphasis on magnetostructural coupling and phase transitions for the design of advanced energy and magnetic materials.*

## 1 Introduction

Cooling and heating account for a significant portion of global energy consumption, which continues to increase due to climate change and global warming.<sup>1,2</sup> Current refrigeration methods rely on greenhouse gases that have severe environmental impacts, including ozone layer depletion and global warming.<sup>3</sup> The magnetocaloric effect (MCE) is a promising alternative for next-generation refrigeration, offering high efficiency and environment-friendliness.<sup>4,5</sup> Conventional magnetocaloric materials undergo heating and cooling upon applying and removing an external magnetic field in an adiabatic process, as illustrated in Fig. 1(a). Two key parameters characterize the magnetocaloric effect: the isothermal entropy change ( $\Delta S$ ) and the adiabatic temperature change ( $\Delta T_{\text{ad}}$ ). The isothermal entropy change, defined as  $\Delta S(H_{\text{ext}}, T) = S(H_{\text{ext}}, T) - S(0, T)$ , represents the entropy difference between states III and I (with and without the external magnetic field) and determines the amount of heat that can be utilized for cooling in one cycle. In conventional magnetocaloric materials, the dominant

<sup>a</sup>Advanced Institute for Materials Research (WPI-AIMR), Tohoku University, Sendai 980-8577, Japan. E-mail: tran.ba.hung.a6@tohoku.ac.jp; li.hao.b8@tohoku.ac.jp

<sup>b</sup>Divisions of Materials and Manufacturing Science, Graduate School of Engineering, Osaka University, 2-1 Yamada-oka, Suita, Osaka 565-0871, Japan

<sup>c</sup>Center for Spintronics Research Network, Osaka University, Toyonaka, Osaka 560-8531, Japan

<sup>d</sup>Institute for Chemical Research, Kyoto University, Uji, Kyoto, 611-0011, Japan



contribution to  $\Delta S$  arises from the magnetic or spin component, denoted as  $\Delta S_{\text{mag}}$ . This typically follows a second-order phase transition, leading to a limited entropy change.<sup>4</sup>

On the other hand, a first-order structural phase transition can be coupled with a magnetic phase transition, forming a magnetostructural coupling.<sup>6,7</sup> The transition from a low-temperature to a high-temperature structure alters the electronic structure and magnetic properties, where the structural transition occurs below the Curie temperature of the low-temperature phase but above that of the high-temperature phase.<sup>7,8</sup> In such cases, the first-order magnetic phase transition from a ferromagnetic low-temperature phase to a paramagnetic high-temperature phase results in a giant isothermal magnetic entropy change, which can be estimated using the Maxwell relations from isothermal magnetization curves.<sup>7,8</sup> However, when charge, spin, and lattice degrees of freedom are coupled, additional contributions from lattice and electronic entropy become significant,<sup>9–11</sup> as illustrated in Fig. 1(b). In this scenario, the isothermal entropy change ( $\Delta S$ ) is not solely determined by the magnetic component ( $\Delta S_{\text{mag}}$ ) but is instead the sum of magnetic, lattice, and electronic contributions:

$$\Delta S = \Delta S_{\text{lat.}} + \Delta S_{\text{ele.}} + \Delta S_{\text{mag.}} \quad (1)$$

Estimating  $\Delta S$  while accounting for lattice, electronic, and magnetic contributions remains a challenging task in both experimental and theoretical simulations.

$\text{BiCu}_3\text{Cr}_4\text{O}_{12}$  is a transition-metal oxide that exhibits a peculiar charge disproportionation effect.<sup>9–11</sup> The cubic structure, which serves as the high-temperature phase with space group  $Im\bar{3}$ , contains a single type of Cr ion with a charge state of +3.75.<sup>11</sup> In contrast, the monoclinic structure corresponding to the low-temperature phase, with space group  $C2/m$ , contains

three distinct types of Cr ions: one with a charge state of +4 and two with charge states of +3.5,<sup>11</sup> as shown in Fig. 2. This material undergoes a first-order magnetic phase transition that is accompanied by a structural change from the cubic to the monoclinic phase, as well as charge disproportionation in the electronic structure.<sup>9–11</sup>

$\text{NdCu}_3\text{Fe}_4\text{O}_{12}$  is a related transition-metal oxide that also exhibits a giant caloric effect, primarily due to charge disproportionation. However, its structure remains stable in the  $Im\bar{3}$  space group across a wide temperature range. In contrast,  $\text{BiCu}_3\text{Cr}_4\text{O}_{12}$  exhibits a first-order magnetostructural transition from a ferromagnetic  $C2/m$  phase to a paramagnetic  $Im\bar{3}$  phase. This structural transformation can be controlled by an external magnetic field, making it suitable for magnetocaloric applications. On the other hand,  $\text{NdCu}_3\text{Fe}_4\text{O}_{12}$  undergoes a magnetic phase transition from an antiferromagnetic to a non-magnetic state, where the local magnetic moment of Fe disappears at the critical temperature. Since both the antiferromagnetic and non-magnetic states are less responsive to magnetic fields, external pressure is typically required to induce the transition—characterizing it as a barocaloric effect.

Although previous experimental studies have reported giant isothermal magnetic entropy changes ( $\Delta S_{\text{mag}}$ ) in  $\text{BiCu}_3\text{Cr}_4\text{O}_{12}$  using the Maxwell relations,<sup>9,10</sup> the contributions from lattice ( $\Delta S_{\text{lat.}}$ ) and electronic ( $\Delta S_{\text{ele.}}$ ) degrees of freedom to the total isothermal entropy change ( $\Delta S$ ) remain unexplored in both experimental and theoretical studies.

This knowledge gap motivates us to investigate the underlying mechanisms and clarify the contributions of lattice and electronic effects to the isothermal entropy change in  $\text{BiCu}_3\text{Cr}_4\text{O}_{12}$ , where charge, spin, and lattice interactions are strongly correlated. To this end, we perform first-principles calculations based on density functional theory (DFT) to determine the

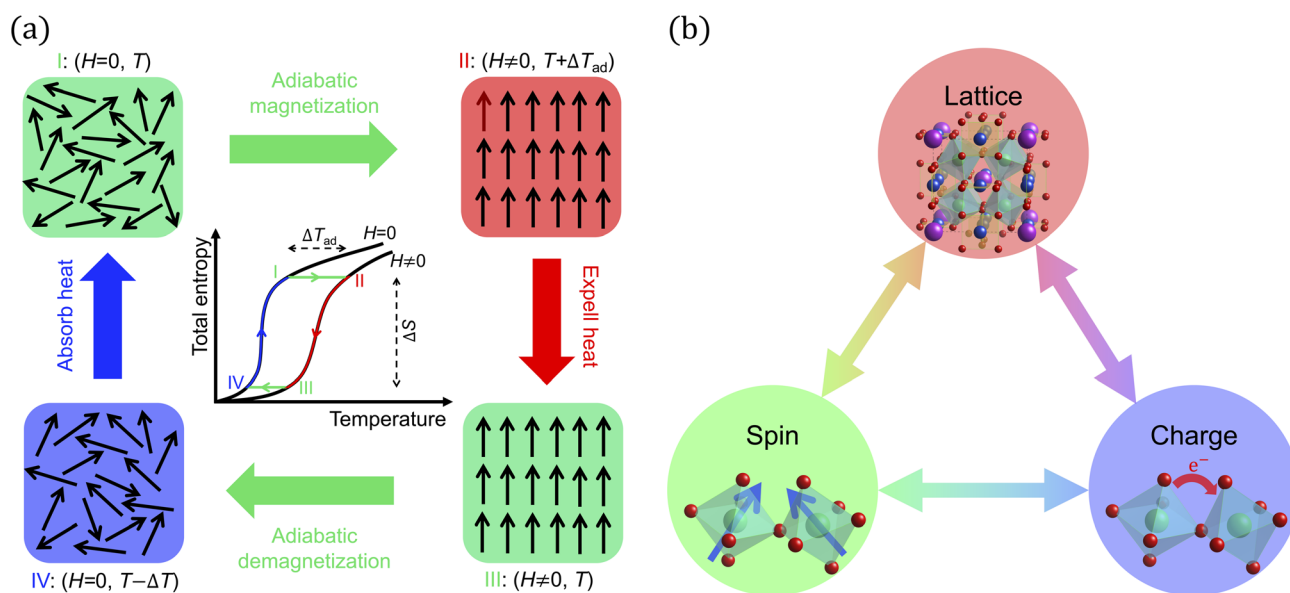


Fig. 1 (a) Diagram of the conventional magnetocaloric effect (a) showing the full cycle of a magnetocaloric material under an external magnetic field, including the isothermal and adiabatic processes. (b) Diagram of spin–lattice–charge coupling that can enhance the magnetocaloric effect, illustrating how interactions between the spins, lattice, and charge are strongly correlated.



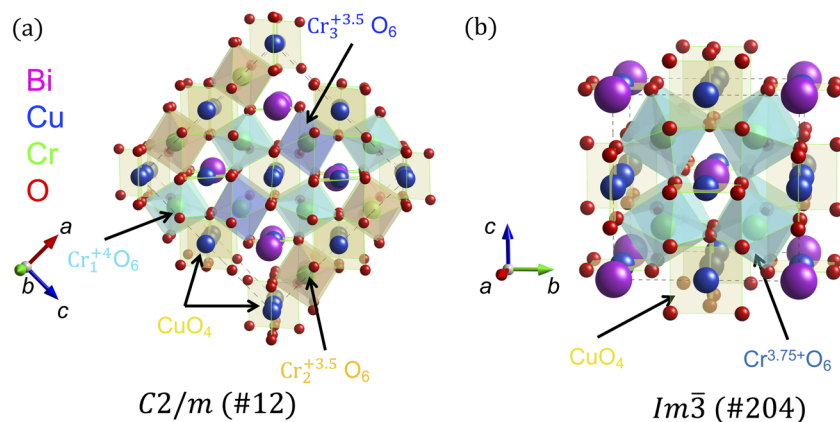


Fig. 2 Crystal structure of the low-temperature phase with space group  $C2/m$  (#12) (a) and high-temperature phase with space group  $Im\bar{3}$  (#204) (b) of  $\text{BiCu}_3\text{Cr}_4\text{O}_{12}$ .<sup>11</sup> The Bi, Cu, Cr, and O atoms are denoted as purple, blue, green, and red colors, respectively.

electronic structure and phonon properties. Additionally, the magnetic exchange coupling constants  $J_{ij}$  are derived using the Liechtenstein formula within the framework of linear response theory.<sup>12</sup> The classical Heisenberg model is then employed to study the magnetic properties of both the  $C2/m$  and  $Im\bar{3}$  phases, using parameters obtained from first-principles calculations.

Our simulation approach is based on the classical Heisenberg model, which incorporates various magnetic interactions with parameters derived from first-principles calculations. These include isotropic exchange coupling ( $J_{ij}$ ), Dzyaloshinskii–Moriya interactions, magnetocrystalline anisotropy energy, and external magnetic fields. In our previous work, we successfully applied this methodology to investigate the spin reorientation mechanism and anisotropic magnetocaloric effect in  $\text{Nd}_2\text{Fe}_{14}\text{B}$ , a system with localized 4f electrons in Nd.<sup>13</sup> That study revealed that the competition between Dzyaloshinskii–Moriya interactions and magnetic anisotropy underlies these phenomena. These results suggest that our computational framework is also applicable to electron-localized magnetic systems such as rare-earth-based compounds, provided that appropriate interaction parameters are used.

To account for the first-order structural phase transition, we incorporate a mixed-phase model based on our earlier work.<sup>8</sup> The isothermal magnetic entropy change is computed from isothermal magnetization curves using the Maxwell relations, consistent with previous experimental studies.<sup>9,10</sup> Furthermore, we calculate the total specific heat and entropy for the pure  $C2/m$  and  $Im\bar{3}$  phases, as well as for the mixed phase, taking into account contributions from lattice, electronic, and magnetic degrees of freedom. Although the isothermal magnetic entropy change is obtained from the Maxwell relations, the total isothermal entropy change of  $\text{BiCu}_3\text{Cr}_4\text{O}_{12}$  is also evaluated using the Clausius–Clapeyron equation based on specific heat calculations. Our results reveal that the lattice and electronic contributions to the isothermal entropy change are substantial. This study thus provides an accurate methodology for investigating the magnetocaloric properties of  $\text{BiCu}_3\text{Cr}_4\text{O}_{12}$  and highlights its potential for application in high-power, high-

efficiency, and environmentally friendly thermal control systems.

## 2 Computational details

The crystal structure parameters of  $\text{BiCu}_3\text{Cr}_4\text{O}_{12}$  for the low-temperature phase ( $C2/m$ ) and high-temperature phase ( $Im\bar{3}$ ) from experimental studies are used for the simulations.<sup>11</sup> The electronic structures of  $\text{BiCu}_3\text{Cr}_4\text{O}_{12}$  in both the  $C2/m$  and  $Im\bar{3}$  phases are investigated using the Vienna *Ab initio* Simulation Package (VASP).<sup>14–16</sup> These calculations employ the generalized gradient approximation, specifically the Perdew–Burke–Ernzerhof (GGA-PBE) functional.<sup>17</sup> For electronic structure calculations, a  $k$ -point mesh of  $3 \times 4 \times 3$  and  $6 \times 6 \times 6$  was utilized for  $C2/m$  and  $Im\bar{3}$  phases, respectively. A plane-wave basis set cutoff energy of 500 eV was used for electronic structure calculations. To compute the force constants, density functional perturbation theory is applied within the VASP framework, using supercells of sizes  $1 \times 1 \times 1$  and  $1 \times 2 \times 2$  for the  $C2/m$  and  $Im\bar{3}$  phases, respectively.<sup>14–16,18,19</sup> The Phonopy code is used to generate these supercells.<sup>18,19</sup> The phonon dispersion curves and phonon density of states are obtained from the computed force constants using Phonopy.<sup>18,19</sup> Additionally, the lattice-specific heat is calculated within the harmonic approximation using Phonopy.<sup>18,19</sup>

The magnetic exchange coupling constants ( $J_{ij}^m$ ) for the classical Heisenberg model are determined using the Liechtenstein formula, as implemented in the Machikaneyama code.<sup>12,20</sup>

The magnetostructural model with a mixed-phase approach is adopted based on our previous work, incorporating the classical Heisenberg model for the magnetic part of the  $C2/m$  and  $Im\bar{3}$  phases.<sup>8,21,22</sup> Meanwhile, the structural transition is described using a modified Potts model.<sup>8</sup>

The classical Heisenberg model for the  $C2/m$  and  $Im\bar{3}$  phases is given as:<sup>21,22</sup>

$$H_{\text{magnetic}} = -\sum_{\langle ij \rangle} J_{ij}^m \vec{S}_i \cdot \vec{S}_j - g\mu_B \sum_i \vec{H}_{\text{ext}} \cdot \vec{S}_i, \quad (2)$$



where the first term represents the exchange interaction between spin  $S_i$  at site  $i$  and spin  $S_j$  at site  $j$ , with  $J_{ij}^m$  denoting the magnetic exchange coupling constants. A positive  $J_{ij}^m$  favors parallel alignment of neighboring spins, while a negative  $J_{ij}^m$  favors antiparallel alignment. The second term corresponds to the Zeeman interaction, where the spin  $S_i$  aligns with the external magnetic field direction to minimize energy. The thermal energy in the classical Heisenberg model is corrected by incorporating the quantum fluctuation–dissipation relations (QFDR), which improves the temperature dependence of magnetization and magnetic-specific heat.<sup>23,24</sup>

To account for the lattice phase transition from the  $C2/m$  to the  $Im\bar{3}$  structure under the influence of magnetic field and temperature, we employ the modified Potts model from our previous work:<sup>8</sup>

$$H_{\text{lattice}} = -\sum_{\langle ij \rangle} \left( J_{ij}^s + K g \mu_B H_{\text{ext}} \right) \delta_{\sigma_i, \sigma_j}, \quad (3)$$

Here,  $J_{ij}^s$  represents the structural coupling constant between the deformation states at sites  $i$  ( $\sigma_i$ ) and  $j$  ( $\sigma_j$ ), while  $K$  is a dimensionless magnetostructural coefficient. The structural coupling constant is directly related to the structural transformation temperature ( $T_{\text{structure}}$ ). In this study, the structural coupling constant is determined based on the magnetization curve from experimental data.<sup>9,10</sup> The second term accounts for the effect of the magnetic field on structural transformation, where one structural phase becomes more favorable under the application of an external magnetic field. A positive  $K$  stabilizes the  $C2/m$  phase in the presence of a magnetic field, whereas a negative  $K$  favors the  $Im\bar{3}$  phase. The experimentally estimated values for  $J_{ij}^s$  and  $K$  are 3.86 meV and 3.0, respectively.<sup>9,10</sup>

To consider the magnetic and structural phase transitions in Monte Carlo simulations, three simulation boxes are used. The size of the supercells for the magnetic part with the classical Heisenberg model is  $8 \times 8 \times 8$  and  $12 \times 12 \times 12$  for  $C2/m$  and  $Im\bar{3}$  phases, respectively. The number of Monte Carlo steps is 100 000, and the first 50 000 steps are discarded.

The total magnetization, including contributions from both phases, is given by:

$$m_{\text{total}} = m(C2/m) \cdot \sigma + m(Im\bar{3}) \cdot (1 - \sigma), \quad (4)$$

Here,  $m(C2/m)$  and  $m(Im\bar{3})$  represent the magnetization of the  $C2/m$  and  $Im\bar{3}$  phases, respectively. The magnetization of each phase is calculated as the summation of the spin vectors in each phase using the classical Heisenberg model, as given in eqn (2).  $\sigma$  is the order parameter of the third simulation box, which is described by eqn (3), where  $\sigma$  and  $1 - \sigma$  represent the concentrations of the  $C2/m$  and  $Im\bar{3}$  phases, respectively.

The isothermal magnetic entropy change can be calculated from the magnetization curve using the Maxwell relations:<sup>8,21,22</sup> Here,  $m_{\text{total}}$  represents the total magnetization, which includes contributions from both the  $C2/m$  and  $Im\bar{3}$  phases, as shown in eqn (4). The total magnetization is associated with the lattice phase transition, which can contribute to a giant isothermal magnetic entropy change in the Maxwell relations.<sup>8</sup>

Furthermore, the total entropy of the  $C2/m$  and  $Im\bar{3}$  phases, considering contributions from the lattice, electronic, and magnetic components, is estimated as:

$$S_{\text{total}}(H_{\text{ext}}, T) = \int_0^T \frac{C_{\text{lat.}}(H_{\text{ext}}, T') + C_{\text{ele.}}(H_{\text{ext}}, T') + C_{\text{mag.}}(H_{\text{ext}}, T')}{T'} dT' \quad (6)$$

Here,  $C_{\text{lat.}}$ ,  $C_{\text{ele.}}$ , and  $C_{\text{mag.}}$  represent the lattice, electronic, and magnetic specific heat, respectively. As mentioned earlier,  $C_{\text{lat.}}$  is calculated from the phonon density of states using the Phonopy code, while  $C_{\text{ele.}}$  is derived from the electronic density of states at the Fermi level.<sup>18,19,25</sup> The magnetic specific heat is calculated as the derivative of the magnetic energy from the classical Heisenberg model in Monte Carlo simulations.<sup>23,24</sup>

It is important to note that the thermal energy of the magnetic component is corrected by applying the quantum fluctuation–dissipation relations (QFDRs), so the magnetic specific heat approaches zero at 0 K, instead of the  $1.0 k_B$  per atom predicted by the equipartition theorem for the classical Heisenberg model with the Boltzmann distribution.<sup>23,24</sup>

The total entropy of the mixed phases is calculated as:

$$S_{\text{total}}^{\text{mix}} = S_{\text{total}}^{C2/m} \cdot \sigma + S_{\text{total}}^{Im\bar{3}} \cdot (1 - \sigma) \quad (7)$$

Here,  $S_{\text{total}}^{\text{mix}}$  represents the total entropy, which includes contributions from the  $C2/m$  and  $Im\bar{3}$  phases, as shown in eqn (6). Meanwhile,  $\sigma$  and  $(1 - \sigma)$  represent the concentrations of the  $C2/m$  and  $Im\bar{3}$  phases, respectively.

The isothermal entropy change can be calculated using the Clausius–Clapeyron equation:

$$\Delta S_{C-C}(H_{\text{ext}}, T) = \Delta S(H_{\text{ext}}, T) = S_{\text{total}}^{\text{mix}}(H_{\text{ext}}, T) - S_{\text{total}}^{\text{mix}}(0, T) \quad (8)$$

### 3 Results and discussion

The electronic density of states of the  $C2/m$  and  $Im\bar{3}$  phases is shown in Fig. 3(a and b). The magnetic configuration in both the  $C2/m$  and  $Im\bar{3}$  phases is ferrimagnetic. The main contribution to saturation magnetization comes from the magnetic

$$\Delta S_M(H_{\text{ext}}, T) = \Delta S_{\text{mag.}}(H_{\text{ext}}, T) = \int_0^{H_{\text{ext}}} \left( \frac{\partial m_{\text{total}}(H, T)}{\partial T} \right) dH \cong \sum_{j=0}^N \frac{m_{\text{total}}(H_j, T + \Delta T) - m_{\text{total}}(H_j, T - \Delta T)}{2\Delta T} \Delta H, \quad (5)$$



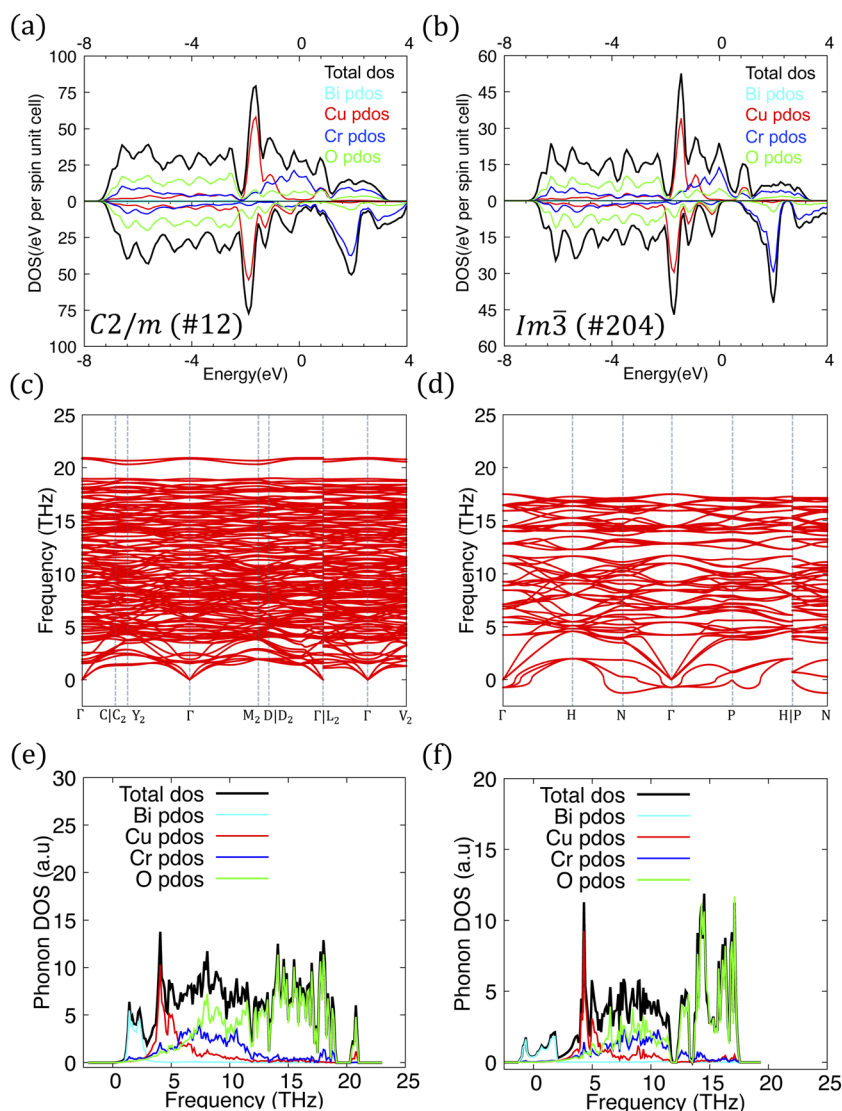


Fig. 3 The electronic density of states (DOS) of  $C2/m$  (a) and  $Im\bar{3}$  (b), where the total DOS, Bi partial DOS, Cu partial DOS, Cr partial DOS, and O partial DOS are represented by black, cyan, red, blue, and green curves, respectively. The phonon dispersion curves of  $C2/m$  (c) and  $Im\bar{3}$  (d) in the high symmetry  $k$ -paths in the Brillouin zone. The phonon density of states (DOS) of  $C2/m$  (e) and  $Im\bar{3}$  (f), where the total DOS, Bi partial DOS, Cu partial DOS, Cr partial DOS, and O partial DOS are represented by black, cyan, red, blue, and green curves, respectively.

moment of Cr atoms, while the magnetic moment of Cu atoms is smaller and antiparallel to that of the Cr atoms. In the  $C2/m$  phase, the magnetic moment of Cr atoms ranges from 1.886 to 2.373  $\mu_B$  per atom as shown in Table 1, while the magnetic moment of Cu atoms ranges from 0.338 to 0.455  $\mu_B$  per atom, oriented opposite to that of the Cr atoms. In the  $Im\bar{3}$  phase, the magnetic moment of Cr atoms is 2.098  $\mu_B$  per atom as shown in Table 1, while the magnetic moment of Cu atoms is 0.443  $\mu_B$  per atom and antiparallel to the Cr magnetic moment. The magnetic moment of Cr atoms exhibits a charge disproportionation effect, with two  $Cr^{4+}$  (with the magnetic moment being 2.373  $\mu_B$  per atom) and two  $Cr^{3.5+}$  ions (with the magnetic moments being 1.886 and 1.896  $\mu_B$  per atom) in the  $C2/m$  phase, while the  $Im\bar{3}$  phase contains only  $Cr^{3.75+}$  (with the magnetic moment being 2.098  $\mu_B$  per atom) ions. This charge disproportionation is also reflected in the density of states, where the

Table 1 Magnetic moments of Cr atoms of  $C2/m$  and  $Im\bar{3}$  with charge disproportionation effect by using VASP

$C2/m$ (#12)			$Im\bar{3}$ (#204)
$Cr_1^{4+}$ ( $\mu_B$ per atom)	$Cr_{2+3.5}$ ( $\mu_B$ per atom)	$Cr_{3+3.5}$ ( $\mu_B$ per atom)	$Cr_{3.75}$ ( $\mu_B$ per atom)
2.373	1.886	1.896	2.098

density of states of Cr atoms in the  $C2/m$  phase is not degenerate, unlike in the  $Im\bar{3}$  phase. Additionally, the electronic structure of the  $Im\bar{3}$  phase shows half-metallic behavior, while the  $C2/m$  phase exhibits a finite density of states in the minority spin channel at the Fermi level. As mentioned earlier, the



electronic-specific heat is calculated from the density of states at the Fermi level for both the  $C2/m$  and  $Im\bar{3}$  phases.

The phonon dispersion and phonon density of states for the  $C2/m$  and  $Im\bar{3}$  phases are shown in Fig. 3(c–f). In the  $C2/m$  phase, there are no soft modes, with all bands lying above zero frequency. In contrast, the  $Im\bar{3}$  phase exhibits soft modes with imaginary frequencies at the  $\Gamma$ ,  $N$ , and  $P$   $k$ -points. From the partial density of states, these soft modes originate from the acoustic bands of Bi atoms in the  $Im\bar{3}$  phase. This observation is consistent with experimental results, where the  $Im\bar{3}$  phase is unstable at 0 K but becomes thermodynamically stable at finite temperatures.<sup>9–11</sup> As mentioned earlier, the lattice-specific heat is calculated from the phonon density of states for both the  $C2/m$  and  $Im\bar{3}$  phases. Additionally, the entropy of the lattice and electronic parts for both phases is integrated from the respective specific heats. However, this entropy calculation uses the reference state as ferromagnetic at 0 K and without an external magnetic field, so the magnetic field does not affect the entropy of the lattice and electronic components of each phase. Instead, the external magnetic field influences the lattice and electronic entropy in the mixed phases, as described in eqn (7).

The magnetic exchange coupling constants for the  $C2/m$  and  $Im\bar{3}$  phases, calculated using the Machikaneyama code, are shown in Fig. 4(a and b). The magnetic exchange coupling constants between Cu and Cr pairs for the first-nearest neighbors are negative in both  $C2/m$  and  $Im\bar{3}$  phases. This indicates that the Cu magnetic moment tends to align antiparallel to the Cr magnetic moment, resulting in a ferrimagnetic configuration, which is consistent with the results obtained from VASP calculations. In contrast, the magnetic exchange coupling constants for the first- and second-nearest-neighbor Cr–Cr pairs are negative in the  $Im\bar{3}$  phase. In the lower-symmetry  $C2/m$  phase, however, these coupling constants exhibit fluctuations and include several large positive values. As a result, the average  $J_{ij}$  values for both the first- and second-nearest-neighbor Cr–Cr pairs in the  $C2/m$  phase are higher than those in the  $Im\bar{3}$  phase. As a result of the enhanced coupling constants in the  $C2/m$  phase, the Curie temperatures, estimated using the mean-field approximation (MFA), are 279.4 K for the  $C2/m$  phase and 203.4

K for the  $Im\bar{3}$  phase. It is important to note that the Curie temperature predicted by MFA is typically overestimated when compared to the values obtained from Monte Carlo simulations.

The temperature dependence of the order parameters in simulations without an external magnetic field is shown in Fig. 4(c). The Curie temperatures of the  $C2/m$  and  $Im\bar{3}$  phases in the Monte Carlo simulations are 195 K and 112 K, respectively. In the absence of structural transformation, the magnetic phase transitions in both  $C2/m$  and  $Im\bar{3}$  phases occur from ferromagnetic to paramagnetic (FM–PM) and are classified as second-order phase transitions. It is important to note that the magnetization curves of the  $C2/m$  ( $m(C2/m)$ ) and  $Im\bar{3}$  ( $m(Im\bar{3})$ ) phases in Monte Carlo simulations have been corrected and become steeper at the Curie temperature compared to classical simulations by considering the Bose–Einstein distribution for magnons, as described by the quantum fluctuation–dissipation relation (QFDR). However, the magnetic phase transition in both  $C2/m$  and  $Im\bar{3}$  phases still remains a second-order phase transition. On the other hand, the structural order parameter  $\sigma$  exhibits a first-order phase transition at a critical temperature between the Curie temperatures of the  $C2/m$  and  $Im\bar{3}$  phases. In this case, at the critical temperature of the structure, the total magnetization  $m_{\text{total}}$  is linked to the first-order phase transition of the structure, with the transition from the ferromagnetic  $C2/m$  phase to the paramagnetic  $Im\bar{3}$  phase. This results in a first-order phase transition in the total magnetization. The structural coupling constant  $J_{ij}^{\sigma}$ , which is proportional to the critical temperature of the structure, is estimated from the experimental magnetization curve to reproduce the slope of the magnetization curve.<sup>9,10</sup>

The temperature and magnetic field dependence of the magnetization in the  $C2/m$  and  $Im\bar{3}$  phases from simulations are shown in Fig. 5(a and b). The magnetization in the  $C2/m$  and  $Im\bar{3}$  phases exhibits second-order phase transition behavior, with a smooth transition from ferromagnetic to paramagnetic at the Curie temperature. Moreover, the application of an external magnetic field results in an increase in the transition temperature, with a smoother slope in the magnetization curve.

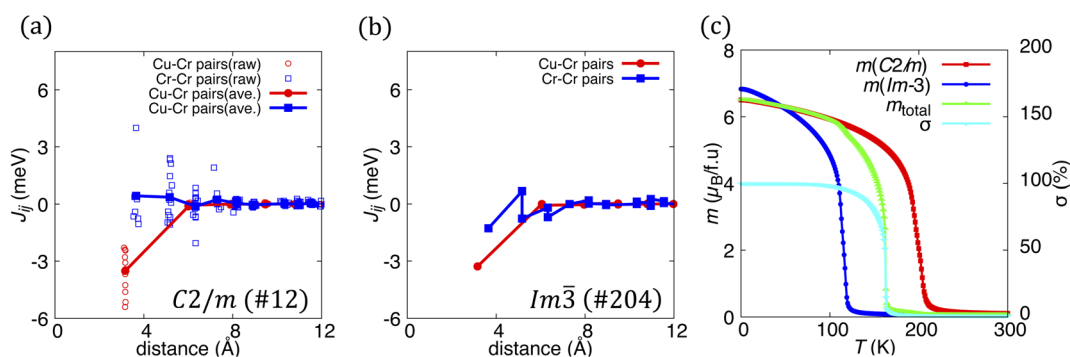


Fig. 4 Magnetic exchange coupling constants ( $J_{ij}$ ) as a function of distance for the  $C2/m$  (a) and  $Im\bar{3}$  (b) phases. Red circles and blue squares represent Cu–Cr and Cr–Cr pairs, respectively. In the  $C2/m$  phase, open symbols indicate raw data, while closed symbols indicate averaged values. (c) Temperature dependence of the order parameters obtained from Monte Carlo simulations. The red, blue, cyan, and green curves correspond to  $m(C2/m)$ ,  $m(Im\bar{3})$ ,  $\sigma$ , and  $m_{\text{total}}$ , respectively.



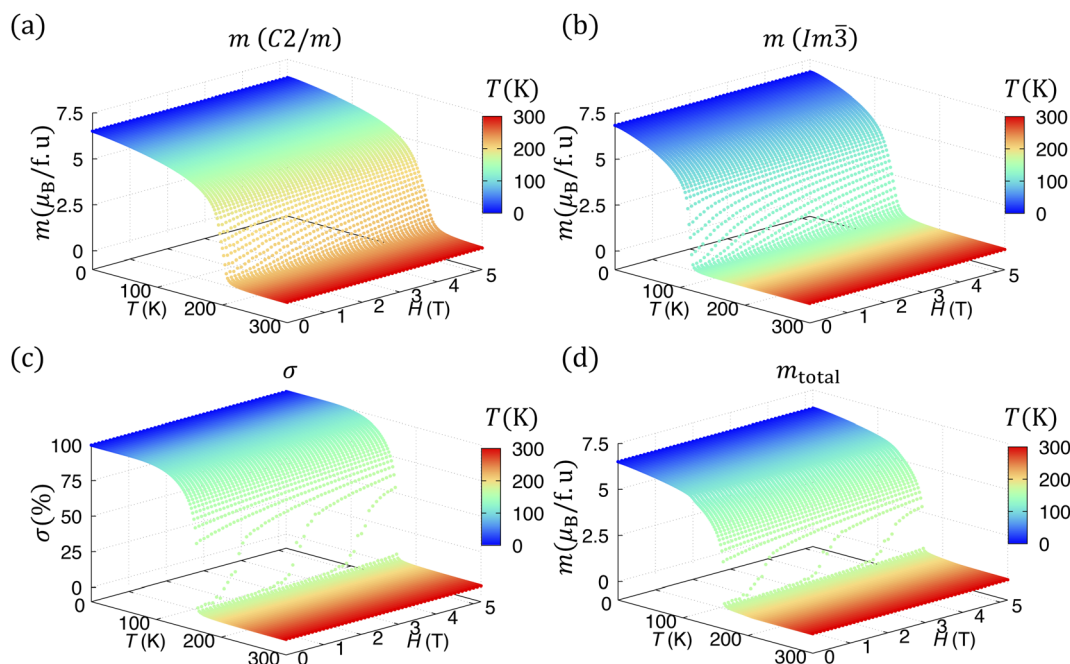


Fig. 5 Temperature and magnetic field dependence of  $m(C2/m)$  (a),  $m(Im\bar{3})$  (b),  $\sigma$  (c), and  $m_{total}$  (d). The color of data points corresponds to the temperature, ranging from 0 K (blue) to 300 K (red).

On the other hand, the order parameter of the structural part  $\sigma$  is shown in Fig. 5(c), which demonstrates first-order phase transition behavior when a finite magnetic field is applied. The

application of an external magnetic field leads to an increase in the transition temperature from the  $C2/m$  to the  $Im\bar{3}$  phase. This is because the magnetization of the  $C2/m$  phase is large (at

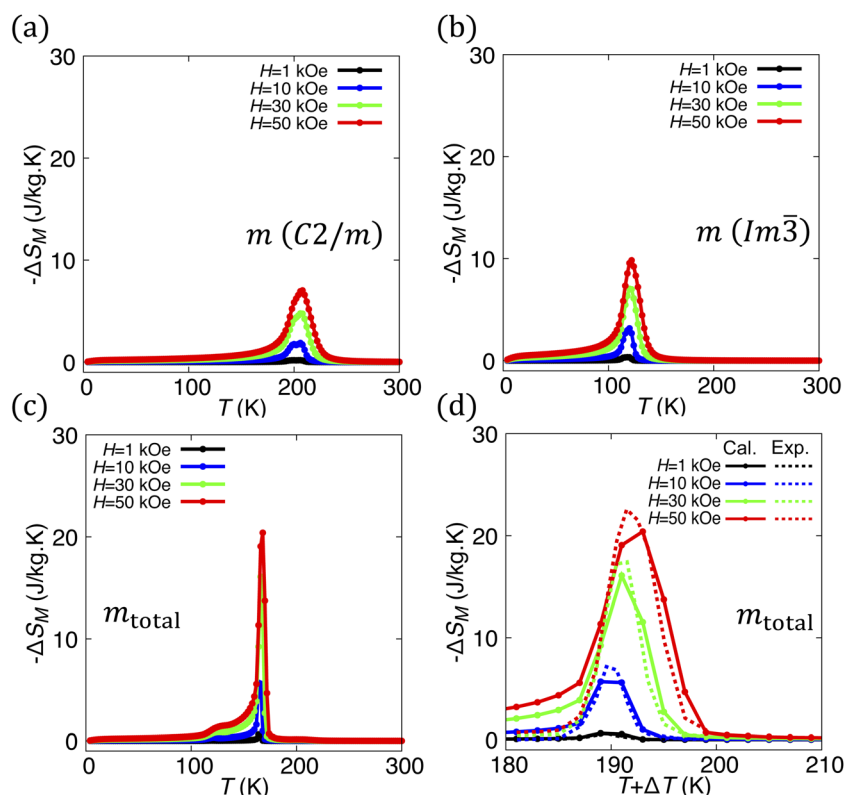


Fig. 6 Isothermal magnetic entropy change of 1 kOe (black), 10 kOe (blue), 30 kOe (green), and 50 kOe (red) from Maxwell relations of  $m(C2/m)$  (a),  $m(Im\bar{3})$  (b), and  $m_{total}$  (c and d). Note that the temperature of the calculation data (solid point lines) in (d) is shifted by  $\Delta T = 30$  K for comparison with experimental data (dashed lines).<sup>9,10</sup>



temperatures below the Curie temperature of the  $C2/m$  phase), while the magnetization of the  $Im\bar{3}$  phase is negligible (at temperatures above the Curie temperature of the  $Im\bar{3}$  phase). In such cases, the total magnetization, shown in Fig. 5(d), exhibits a first-order phase transition at a finite applied magnetic field, as it is associated with the structural transition as described in eqn (4). Since the magnetization of both the  $C2/m$  and  $Im\bar{3}$  phases is corrected with QFDR, the accuracy of the total magnetization is also improved, as the total magnetization results from the contributions of both the  $C2/m$  and  $Im\bar{3}$  phases.

The isothermal magnetic entropy changes calculated using the Maxwell relations for the  $C2/m$  and  $Im\bar{3}$  phases are shown in Fig. 6(a and b). Due to the second-order phase transition in the magnetization of both  $C2/m$  and  $Im\bar{3}$  phases, the isothermal magnetic entropy change of both phases is broadened and not too high. Note that, with the correction from QFDR, the isothermal magnetic entropy change of both phases approaches zero at 0 K, instead of a finite value as seen in classical simulations. The isothermal magnetic entropy change derived from the Maxwell relations based on the total magnetization of the mixed phases is shown in Fig. 6(c and d). Note that the temperature scale of the calculated data in Fig. 6(d) is shifted by  $\Delta T = 30$  K for comparison with the experimental results.<sup>9,10</sup> The isothermal magnetic entropy change from the calculations in this work is in good agreement with the entropy change in the experimental data.<sup>9,10</sup> This agreement arises because we use the

same method (Maxwell relations) to calculate the isothermal magnetic entropy change, and the simulation model is appropriate for reproducing the entropy change in the material with mixed phases. However, the isothermal magnetic entropy change estimated from the Maxwell relations does not contain all the terms in entropy that can be used for cooling, as the lattice and electronic parts of entropy are not negligible.

On the other hand, we consider another approach (Clausius–Clapeyron equation) to calculate the isothermal entropy change. The specific heat and entropy contributions from the lattice, electronic, and total components under various external magnetic fields for  $C2/m$  and  $Im\bar{3}$  phases are shown in Fig. 7(a, b, d and e). The classical Heisenberg model is known to be inaccurate for describing thermodynamic properties at low temperatures. In particular, it yields a finite magnetic specific heat of  $1.0 k_B$  per atom at 0 K due to the classical equipartition theorem, which contradicts both the third law of thermodynamics and experimental observations. To address this issue, we apply the quantum fluctuation–dissipation relation (QFDR) to the classical Heisenberg model. This approach significantly improves the behavior of spontaneous magnetization and magnetic specific heat, especially in the low-temperature region. It is especially important for accurately estimating the total magnetic entropy, which is obtained by integrating the specific heat. The total specific heat at zero kOe shows a peak at the Curie temperature, while applying an external magnetic

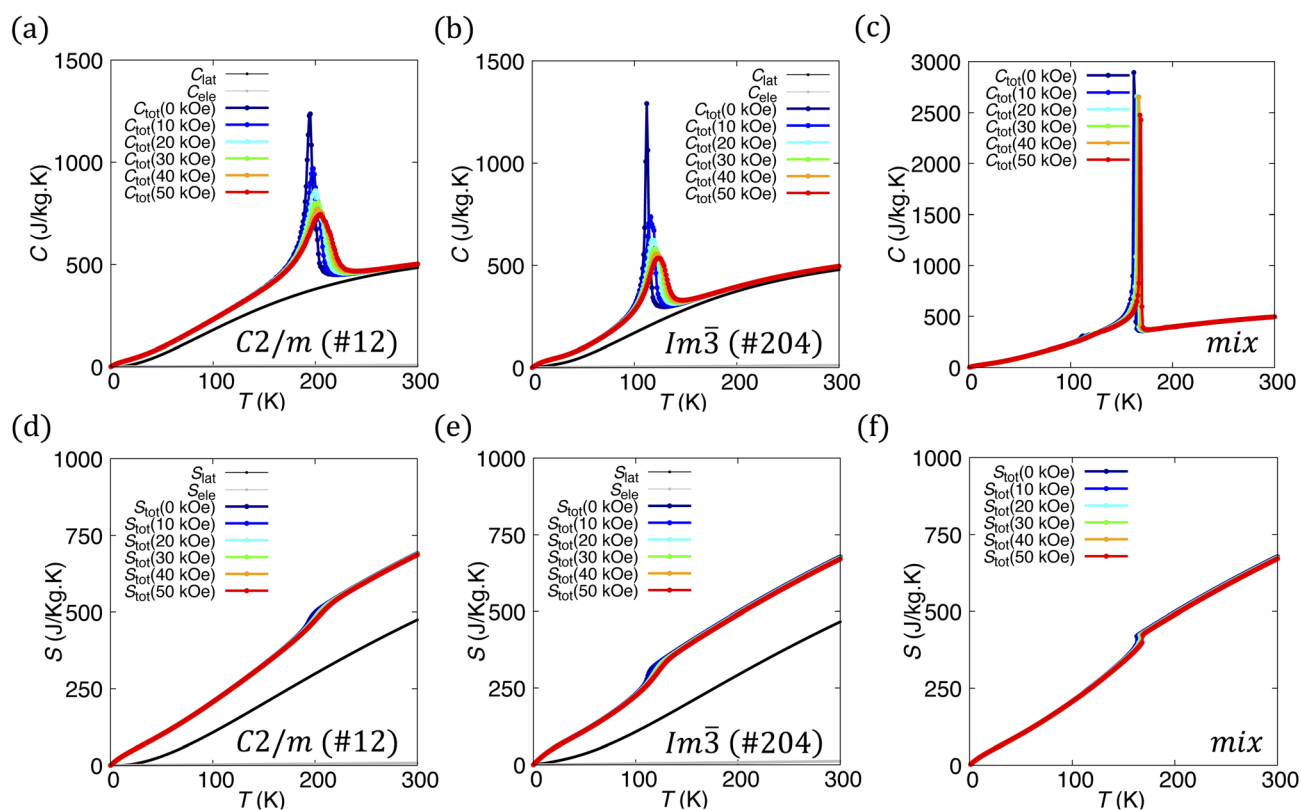


Fig. 7 The specific heat of lattice (black), electronic (gray), and total contributions at 0 kOe (dark blue), 10 kOe (blue), 20 kOe (cyan), 30 kOe (green), 40 kOe (orange), and 50 kOe (red) of  $C2/m$  (a),  $Im\bar{3}$  (b), and mixed phases (c). The entropy of lattice (black), electronic (gray), and total contributions at 0 kOe (dark blue), 10 kOe (blue), 20 kOe (cyan), 30 kOe (green), 40 kOe (orange), and 50 kOe (red) of  $C2/m$  (d),  $Im\bar{3}$  (e), and mixed phases (f).



field broadens the peak and shifts it to the high-temperature side, reflecting the effect of the external magnetic field. The total entropy of both phases is calculated from eqn (5), which increases with temperature and exhibits a jump at the Curie temperature under 0 kOe. Under a finite external magnetic field, the total entropy shifts to the high-temperature side with smoother curves compared to the zero kOe case.

The total specific heat and total entropy of the mixed phases under various external magnetic fields are shown in Fig. 7(c and f). The total entropy of mixed phases is calculated using eqn (7), accounting for contributions from both the  $C2/m$  and  $Im\bar{3}$  phases, with the molar fraction of phase  $C2/m$  being  $\sigma$  and that of the  $Im\bar{3}$  phase being  $1 - \sigma$ . Then, the specific heat of the mixed phases can be extracted as the derivative of the total entropy of the mixed phases with respect to temperature. While the specific heat of pure  $C2/m$  and  $Im\bar{3}$  phases shows small and broadened peaks, typical of a second-order phase transition in magnetization, the specific heat of the mixed phases is very sharp at the critical temperature. From the specific heat of the mixed phases, the isothermal entropy change can be estimated, with contributions from lattice, electronic, and magnetic parts.

The entropy differences between  $C2/m$  and  $Im\bar{3}$  phases are shown in Fig. 8(a). The lattice entropy difference exhibits a peak at low temperatures and changes sign to become negative at

intermediate and high temperatures. Meanwhile, the entropy difference of the electronic part increases linearly over a wide temperature range. The total entropy difference under various external magnetic field strengths has contributions from lattice, electronic, and magnetic components. It increases linearly at low temperatures, with the main contribution coming from the lattice part. However, when the lattice entropy difference reaches its maximum and starts decreasing, changing sign, the total entropy difference remains high with only a slight change due to the contribution from the magnetic part. The total entropy difference then increases significantly and reaches a maximum at the critical temperature of the  $Im\bar{3}$  phase, before decreasing and becoming zero at the critical temperature of the  $C2/m$  phase. Although the total entropy difference provides the maximum entropy between  $C2/m$  and  $Im\bar{3}$  phases, the isothermal entropy change, which relates to the amount of heat that can be used for refrigeration, needs to consider the molar fraction of the  $C2/m$  and  $Im\bar{3}$  phases.

The isothermal entropy changes of the mixed phases at various external magnetic field strengths, derived from the Clausius–Clapeyron equation as eqn (7), are shown in Fig. 8(b). The isothermal entropy changes of mixed phases show a peak at the critical temperatures corresponding to the structural transition from the  $C2/m$  to the  $Im\bar{3}$  phase. The peaks in the

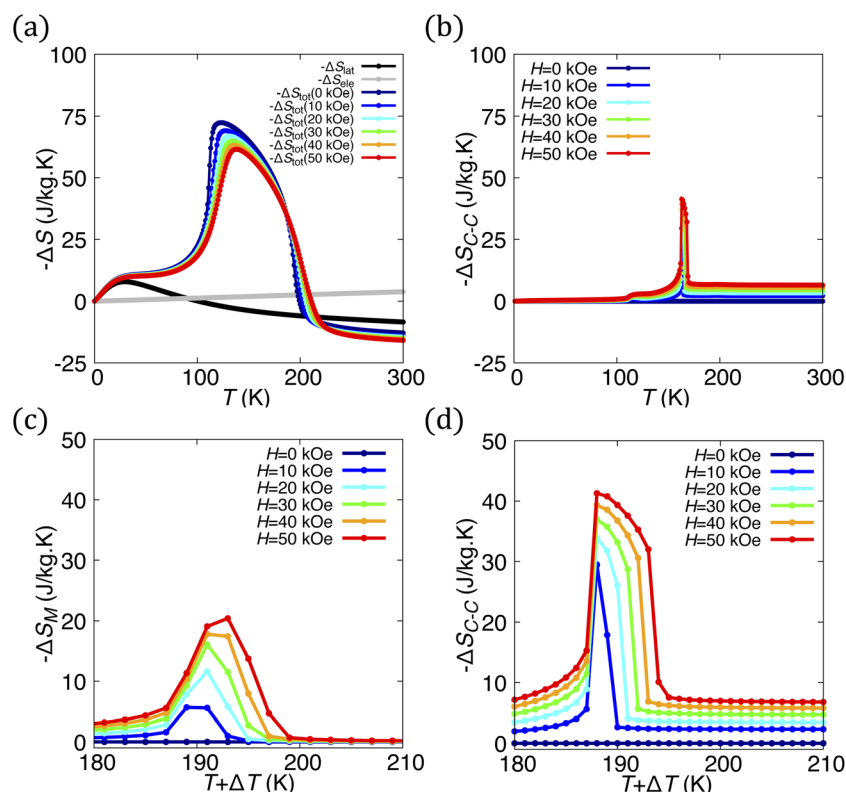


**Fig. 8** (a) The entropy difference between  $C2/m$  and  $Im\bar{3}$  of lattice (black), electronic (gray), and total contributions at 0 kOe (dark blue), 10 kOe (blue), 20 kOe (cyan), 30 kOe (green), 40 kOe (orange), and 50 kOe (red). (b) The isothermal entropy change at 0 kOe (dark blue), 10 kOe (blue), 20 kOe (cyan), 30 kOe (green), 40 kOe (orange), and 50 kOe (red) by using the Clausius–Clapeyron equation. The isothermal magnetic entropy changes and isothermal entropy changes at 0 kOe (dark blue), 10 kOe (blue), 20 kOe (cyan), 30 kOe (green), 40 kOe (orange), and 50 kOe (red) by using Maxwell relations (c) and the Clausius–Clapeyron equation (d), respectively. Note that the temperature in (c and d) is shifted by  $\Delta T = 30$  K for comparison with experimental data.<sup>9,10</sup>



isothermal entropy changes of mixed phases are smaller and narrower than those of the total entropy difference due to the effect of the structural change from the  $C2/m$  to the  $Im\bar{3}$  phase. The isothermal magnetic entropy changes from the Maxwell relations and isothermal entropy changes calculated from the Clausius–Clapeyron equation are shown in Fig. 8(c and d). The isothermal magnetic entropy changes from the Maxwell relations are smaller and less sharp those from the Clausius–Clapeyron equation, especially in the case of an external magnetic field of 10 kOe. This is because the isothermal magnetic entropy change from the Maxwell relations only includes the contribution from the magnetic part. Although magnetization is associated with structural changes through the molar fraction in the total magnetization as in eqn (4), the contributions from lattice and electronic parts are not accounted for. The lattice and electronic contributions to the isothermal entropy change in the Clausius–Clapeyron equation is also associated with structure changes through the molar fraction. Note that the effect of the external magnetic fields on the lattice and electronic parts is not considered in this work, as the phonon and electronic structure calculations were carried out in the ground state without external magnetic fields. However, the effect of external magnetic fields on the lattice and electronic parts of the mixed phases is considered through the molar fraction, which is controlled by the external magnetic field. In this case, the isothermal entropy change calculated using the Clausius–Clapeyron equation is more realistic than that that obtained from Maxwell relations for estimating the amount of heat that can be used for cooling in one cycle of the magnetocaloric effect.

## 4 Conclusion

This study comprehensively investigates the magnetic and thermodynamic properties of  $\text{BiCu}_3\text{Cr}_4\text{O}_{12}$ , which exhibits a low-temperature  $C2/m$  phase and a high-temperature  $Im\bar{3}$  phase, by combining first-principles calculations and Monte Carlo simulations. Phonon calculations reveal soft phonon modes in the  $Im\bar{3}$  phase, originating from Bi atoms, providing insights into its thermodynamic instability at 0 K. Our analysis uncovers the mechanism of the first-order phase transition in both structure and magnetism, where the structural transition due to charge transfer, lattice distortion, and charge disproportionation (from the  $C2/m$  to  $Im\bar{3}$  phase) occurs within the temperature window defined by the Curie temperatures of the two phases. This structural transformation drives a first-order magnetic phase transition from ferromagnetic( $C2/m$ ) to paramagnetic( $Im\bar{3}$ ), which is analyzed using a combination of the classical Heisenberg model and our mixed-phase model. The isothermal magnetic entropy changes obtained from Maxwell relations in this study are in good agreement with experimental findings, validating the accuracy of our mixed phases approach. Furthermore, applying the Clausius–Clapeyron equation provides a more precise assessment of isothermal entropy change, highlighting the crucial roles of lattice and electronic contributions in the magnetocaloric effect. The resulting isothermal entropy change is significantly larger than the isothermal magnetic entropy change with the magnetic part

obtained from Maxwell relations alone. This comprehensive analysis enhances the understanding of magnetocaloric properties in the  $C2/m$  and  $Im\bar{3}$  phases, demonstrating the material's potential for advanced magnetocaloric refrigeration technologies. These findings highlight the intricate interplay between magnetic, structural, and electronic properties in  $\text{BiCu}_3\text{Cr}_4\text{O}_{12}$ , paving the way for the development of next-generation cooling materials.

## Author contributions

H. B. Tran: conceptualization, investigation, funding acquisition, writing – original Draft. H. Li: funding acquisition, resources, writing – review & editing. M. Goto: writing – review & editing. K. Sato: writing – review & editing. Y. Shimakawa: funding acquisition, writing – review & Editing.

## Conflicts of interest

There are no conflicts to declare.

## Data availability

The data that support the findings of this study are available from the corresponding author upon reasonable request.

## Acknowledgements

The authors thank Prof. T. Kato for valuable discussions. This work was partially supported by JSPS KAKENHI under the “Grant-in-Aid for Research Activity Start-up” (Grant Number JP24K22847), “Grant-in-Aid for Early-Career Scientists” (Grant Number JP25K17932), and “Grants-in-Aid for Scientific Research” (Grant Numbers JP23H05457, JP20K20547, JP20H00397, JP22KK0075, and JP23K13814). Additional support was provided by the International Collaborative Research Program of the Institute for Chemical Research, Kyoto University, from MEXT of Japan; Advanced International Collaborative Research Program (AdCORP) (Grant Number JPMJKB2304) and Adopting Sustainable Partnerships for Innovative Research Ecosystem (ASPIRE) (Grant Number JPMJAP2314), through the Japan Science and Technology Agency (JST). Computations were performed on the supercomputers at the Institute for Solid State Physics, University of Tokyo, and on the MASAMUNE-IMR system at the Center for Computational Materials Science, Institute for Materials Research, Tohoku University (Project Numbers 202412-SCKXX-0211 and 202412-SCKXX-0205).

## Notes and references

- 1 G. Falchetta, E. D. Cian, F. Pavanello and I. S. Wing, Inequalities in global residential cooling energy use to 2050, *Nat. Commun.*, 2024, **15**, 7874, DOI: [10.1038/s41467-024-52028-8](https://doi.org/10.1038/s41467-024-52028-8).
- 2 J. Yuan, Z. Jiao, X. Xiao, K. Emura and C. Farnham, Impact of future climate change on energy consumption in residential



- buildings: A case study for representative cities in Japan, *Energy Rep.*, 2024, **11**, 1675, DOI: [10.1016/j.egy.2024.01.042](https://doi.org/10.1016/j.egy.2024.01.042).
- 3 H. Wang, L. Zhao, R. Cao and W. Zeng, Refrigerant alternative and optimization under the constraint of the greenhouse gas emissions reduction target, *J. Cleaner Prod.*, 2021, **296**, 126580, DOI: [10.1016/j.jclepro.2021.126580](https://doi.org/10.1016/j.jclepro.2021.126580).
  - 4 K. A. Gschneidner Jr. and V. K. Pecharsky, Magnetocaloric Materials, *Annu. Rev. Mater. Res.*, 2000, **30**, 387, DOI: [10.1146/annurev.matsci.30.1.387](https://doi.org/10.1146/annurev.matsci.30.1.387).
  - 5 X. Tang, H. Sepehri-Amin, N. Terada, A. Martin-Cid, I. Kurniawan, S. Kobayashi, Y. Kotani, H. Takeya, J. Lai, Y. Matsushita, T. Ohkubo, Y. Miura, T. Nakamura and K. Hono, Magnetic refrigeration material operating at a full temperature range required for hydrogen liquefaction, *Nat. Commun.*, 2022, **13**, 1817, DOI: [10.1038/s41467-022-29340-2](https://doi.org/10.1038/s41467-022-29340-2).
  - 6 J. Liu, Y. Gong, G. Xu, G. Peng, I. A. Shah, N. Hassan and F. Xu, Realization of magnetostructural coupling by modifying structural transitions in MnNiSi-CoNiGe system with a wide Curie-temperature window, *Sci. Rep.*, 2016, **6**, 23386, DOI: [10.1038/srep23386](https://doi.org/10.1038/srep23386).
  - 7 J. Liu, T. Gottschall, K. P. Skokov, J. D. Moore and O. Gutfleisch, Giant magnetocaloric effect driven by structural transitions, *Nat. Mater.*, 2012, **11**, 620, DOI: [10.1038/nmat3334](https://doi.org/10.1038/nmat3334).
  - 8 H. B. Tran, T. Fukushima, K. Sato, Y. Makino and T. Oguchi, Tuning structural-transformation temperature toward giant magnetocaloric effect in MnCoGe alloy: A theoretical study, *J. Alloys Compd.*, 2021, **854**, 157063, DOI: [10.1016/j.jallcom.2020.157063](https://doi.org/10.1016/j.jallcom.2020.157063).
  - 9 Y. Kosugi, M. Goto, Z. Tan, D. Kan, M. Isobe, K. Yoshii, M. Mizumaki, A. Fujita, H. Takagi and Y. Shimakawa, Giant multiple caloric effects in charge transition ferrimagnet, *Sci. Rep.*, 2021, **11**, 12682, DOI: [10.1038/s41598-021-91888-8](https://doi.org/10.1038/s41598-021-91888-8).
  - 10 Y. Shimakawa and Y. Kosugi, Giant caloric effects in charge-spin-lattice coupled transition-metal oxides, *J. Mater. Chem. A*, 2023, **11**, 12695, DOI: [10.1039/d2ta09186k](https://doi.org/10.1039/d2ta09186k).
  - 11 M. Etter, M. Isobe, H. Sakurai, A. Yaresko, R. E. Dinnebier and H. Takagi, Charge disproportionation of mixed-valent Cr triggered by Bi lone-pair effect in the A-site-ordered perovskite BiCu<sub>3</sub>Cr<sub>4</sub>O<sub>12</sub>, *Phys. Rev. B*, 2018, **97**, 195111, DOI: [10.1103/PhysRevB.97.195111](https://doi.org/10.1103/PhysRevB.97.195111).
  - 12 A. I. Liechtenstein, M. I. Katsnelson, V. P. Antropov and V. A. Gubanov, Local spin density functional approach to the theory of exchange interactions in ferromagnetic metals and alloys, *J. Magn. Magn. Mater.*, 1987, **67**, 65, DOI: [10.1016/0304-8853\(87\)90721-9](https://doi.org/10.1016/0304-8853(87)90721-9).
  - 13 H. B. Tran and Y. Matsushita, Dzyaloshinskii–Moriya interactions in Nd<sub>2</sub>Fe<sub>14</sub>B as the origin of spin reorientation and the rotating magnetocaloric effect, *Appl. Mater. Today*, 2023, **32**, 101825, DOI: [10.1016/j.apmt.2023.101825](https://doi.org/10.1016/j.apmt.2023.101825).
  - 14 G. Kresse and J. Hafner, Ab initio molecular dynamics for liquid metals, *Phys. Rev. B: Condens. Matter Mater. Phys.*, 1993, **47**, 558, DOI: [10.1103/PhysRevB.47.558](https://doi.org/10.1103/PhysRevB.47.558).
  - 15 G. Kresse and J. Furthmüller, Efficiency of *ab initio* total energy calculations for metals and semiconductors using a plane-wave basis set, *Comput. Mater. Sci.*, 1996, **6**, 15, DOI: [10.1016/0927-0256\(96\)00008-0](https://doi.org/10.1016/0927-0256(96)00008-0).
  - 16 G. Kresse and J. Furthmüller, Efficient iterative schemes for *ab initio* total-energy calculations using a plane-wave basis set, *Phys. Rev. B: Condens. Matter Mater. Phys.*, 1996, **54**, 11169, DOI: [10.1103/PhysRevB.54.11169](https://doi.org/10.1103/PhysRevB.54.11169).
  - 17 J. P. Perdew, K. Burke and M. Ernzerhof, Generalized gradient approximation made simple, *Phys. Rev. Lett.*, 1996, **77**, 3865, DOI: [10.1103/PhysRevLett.77.3865](https://doi.org/10.1103/PhysRevLett.77.3865).
  - 18 A. Togo, L. Chaput, T. Tadano and I. Tanaka, Implementation strategies in phonopy and phono3py, *J. Phys.: Condens. Matter*, 2023, **35**, 353001, DOI: [10.1088/1361-648X/acd831](https://doi.org/10.1088/1361-648X/acd831).
  - 19 A. Togo, First-principles phonon calculations with phonopy and phono3py, *J. Phys. Soc. Jpn.*, 2023, **92**, 012001, DOI: [10.7566/JPSJ.92.012001](https://doi.org/10.7566/JPSJ.92.012001).
  - 20 H. Akai and P. H. Dederichs, *Phys. Rev. B: Condens. Matter Mater. Phys.*, 1993, **47**, 8739, DOI: [10.1103/PhysRevB.47.8739](https://doi.org/10.1103/PhysRevB.47.8739).
  - 21 H. B. Tran, H. Momida, Y. Matsushita, K. Sato, Y. Makino, K. Shirai and T. Oguchi, Effect of magnetocrystalline anisotropy on magnetocaloric properties of an AlFe<sub>2</sub>B<sub>2</sub> compound, *Phys. Rev. B*, 2022, **105**, 134402, DOI: [10.1103/PhysRevB.105.134402](https://doi.org/10.1103/PhysRevB.105.134402).
  - 22 H. B. Tran, H. Momida, Y. Matsushita, K. Shirai and T. Oguchi, Insight into anisotropic magnetocaloric effect of CrI<sub>3</sub>, *Acta Mater.*, 2022, **231**, 117851, DOI: [10.1016/j.actamat.2022.117851](https://doi.org/10.1016/j.actamat.2022.117851).
  - 23 C. H. Woo, H. Wen, A. A. Semenov, S. L. Dudarev and P. W. Ma, Quantum heat bath for spin-lattice dynamics, *Phys. Rev. B: Condens. Matter Mater. Phys.*, 2015, **91**, 104306, DOI: [10.1103/PhysRevB.91.104306](https://doi.org/10.1103/PhysRevB.91.104306).
  - 24 L. Bergqvist and A. Bergman, Realistic finite temperature simulations of magnetic systems using quantum statistics, *Phys. Rev. Mater.*, 2018, **2**, 013802, DOI: [10.1103/PhysRevMaterials.2.013802](https://doi.org/10.1103/PhysRevMaterials.2.013802).
  - 25 C. Kittel, *Introduction to Solid State Physics*, 8th edn, John Wiley & Sons, Inc., 2005, p. 146.

